

Debinding of additively manufactured parts from spinel powders with particle sizes below 200 nm

Paulina Zubrzycka^{a,b,*}, Marta Radecka^b, Thomas Graule^a, Michael Stuer^{a,**}

^a Laboratory for High Performance Ceramics, Empa, Überlandstrasse 129, 8600 Dübendorf, Switzerland

^b Faculty of Materials Science and Ceramics, AGH University of Science and Technology, al. Adama Mickiewicza 30, 30-059, Krakow, Poland

ARTICLE INFO

Keywords:

Ceramics additive manufacturing
DLP
MgAl₂O₄
Thermal debinding
Nanopowder processing

ABSTRACT

The widespread application of additive manufacturing in ceramics is still hindered by recurrent cracking issues during debinding. To date, the various strategies that have been attempted to reduce this problem often fail upon particle size reduction. Indeed, a reduction in particle size affects the diffusion rates (e.g. pore network) such that even slow heating rates and long dwell times during debinding may not prevent crack formation. In this study, the analysis of the curing and debinding behavior of magnesium aluminate spinel in different acrylates and one methacrylate was performed. Crack formation was analyzed by combining thermal effects with FTIR and dilatometry data. The strategy to reduce exothermal effects through the addition of propylene carbonate (i.e. non-reactive diluent) was evaluated.

1. Introduction

Although shaping complex fine structures is an area where additive manufacturing (AM) has already proven successful, defect-free debinding in parts with larger strut sections or finer powders remains challenging in AM. During this step, crack formation may occur due to both rapid formation of significant amounts of gases (e.g. CO₂, H₂O) and temperature gradients related to the exothermic reactions. Additionally, crack formation was also reported to occur from mechanical stresses that occur during the polymerization of residual monomers at elevated temperatures [1].

Various strategies have been proposed to minimize crack formation during the thermal debinding. An engineering approach suggests the design of complex structures inside large volume parts [2]. When this is not feasible, an alternative approach entails adapting the mechanical properties of the polymer matrix according to the characteristic dimension of the parts: mostly multifunctional (meth)-acrylates used for fine complex structures are replaced with a mixture of difunctional (meth)-acrylates for large volume parts [3]. Thus, in many cases, slurry optimization depends not only on the material and powder characteristics but also on the desired target shape, effectively preventing, to date, true realization of the freedom of shape touted in the AM field.

In an attempt to overcome such shape-dependent slurry optimization

requirements, other strategies are required, such as combining substances which decompose at different temperatures [4] or adding non-reactive diluents such as benzyl alcohol [5], decalin [6] and isopropyl alcohol [7] to smooth gas formation peaks. Some of the reported non-reactive diluents – like PEG – can furthermore act as plasticizers to decrease internal stresses [8,9]. Following the AM step, the cleaning procedure has also been suggested to influence the crack formation during debinding: polyethylene glycol [10], ethyl alcohol [10] or monomer (HDDA) [11] have been reported as cleaning agents. On top of the chemical system fine tuning, the debinding program itself also requires optimization. Better debinding results have been reported with dwell temperatures set based on the onset of the DTG peak and the dwell times set proportionally to the DTG peak depths [12]. Alternatively, the decomposition rate can also be optimized via model-free kinetics and debinding atmosphere changes [13–18]. In particular, crack formation could be reduced combining vacuum debinding with low heating rates (0.5 °C/min), when compared to higher heating rates in air, Ar or 95% Ar + 5% H₂ atmospheres [19]. In many cases, however, optimization of the debinding program involves significant experimental effort without an in-depth evaluation of the underlying mechanisms.

Within the general context of AM, and particularly of debinding, little has been reported about the role of particle size [20,21]. The particle size distribution, however, impacts all process steps, from the

* Corresponding author. Laboratory for High Performance Ceramics, Empa, Überlandstrasse 129, 8600 Dübendorf, Switzerland.

** Corresponding author. Laboratory for High Performance Ceramics, Empa, Überlandstrasse 129, 8600 Dübendorf, Switzerland.

E-mail addresses: paulina.zubrzycka@agh.edu.pl (P. Zubrzycka), michael.stuer@empa.ch (M. Stuer).

slurry formulation to the final sintering. In particular, suitable slurry formulations with particle sizes below 200 nm have only been scarcely reported [22] (150–200 nm Al_2O_3 [23,24], 50 nm ZrO_2 [25], 200 nm Si_3N_4 [26], 200 nm ZrO_2 [27], and 150 nm MgAl_2O_4 [16]). This may be due to the electrostatic stabilization mechanisms in non-aqueous media being less well understood [28] and steric dispersants being mostly optimized for larger particles. Consequently, the lower achievable solid loading with decreasing particle size may negate some of their potential benefits, especially during sintering. Decreasing particle sizes, moreover, also affects the light scattering – which depends on the refractive index mismatch between the particles and the suspending media as well as the relation between particle size and exposure wavelength – during exposure, thereby altering the effective AM resolution [29]. Additionally, decreasing the particle size reduces the critical strut thickness for debinding following a power law (by analogy with injection moulding [30]).

This study aims to elucidate the influence of nanopowders on the AM and the subsequent crack formation during the debinding process. Different difunctional acrylates and one di-methacrylate were chosen and the crack structure evaluated after debinding (and sintering). The results provide a discussion basis for potential crack formation mechanisms based on the process route.

2. Experimental

2.1. Materials and reagents

The powder used in this study was an MgAl_2O_4 spinel (S25CR, Baikowski, France) with a specific surface area $S_{\text{BET}} = 23 \text{ m}^2/\text{g}$. Detailed powder characteristics have been measured and can be found in the results section.

The powder was dispersed using Solsperser 41000 (Lubrizol, USA). Isopropanol (IPA) (Reag. Ph Eur $\geq 99.8\%$, analysis grade EMSURE® ACS, Merck, Germany) was used as a dispersing liquid during the milling of powder with dispersant added. The different acrylates (Miwon Specialty Chemical Co, South Korea), with MeHQ inhibitor content between 50 and 150 ppm, and the methacrylate (Sartomer, Arkema, USA) with MeHQ of 400 ppm used for the subsequent slurry preparation can be found in Table 1. Propylene carbonate (ReagentPlus 99%, Merck, Germany) was used as a non-reactive diluent.

2-hydroxy-2-methyl-1-phenyl-propan-1-one (Irgacure 1173, BASF, Germany) with a quantum yield of 0.38, extinction coefficient $\epsilon_{385} < 1$ was chosen as the photoinitiator [31].

Table 1
Properties of the acrylates and methacrylates used.

Number	Name	Viscosity (mPa·s@25 °C)	Refractive index (n_D^{25})
M201	HDDMA 1,6-Hexanediol Dimethacrylate	1–10	1.456
M205	BDDMA 1,4-Butanediol Dimethacrylate	1–10	1.456
M221	EGDMA Ethylene glycol Dimethacrylate	3–8	1.453
SR210HH	PEG200DMA Polyethylene glycol 200 Dimethacrylate	12–15	1.461
M200	HDDA 1,6-Hexanediol Diacylate	5–15	1.455
M2010	DDDA 1,10-Decanediol Diacylate	7–15	1.458
M282	PEG200DA Polyethylene glycol 200 Diacylate	15–35	1.463
M300	1,4-Butandiol Diacylate	5	1.456
	TMPTA Trimethylolpropane Triacylate	80–120	1.473
M410	DTMPTTA Ditrimethylolpropane Tetraacylate	450–750	1.476

2.2. Slurry preparation and additive manufacturing

First, different amounts of dispersing agents (1 wt%, 3 wt%, 5 wt% and 7 wt% per powder mass) were added to 25 vol% spinel in isopropanol to identify the optimal dispersant concentration and milling time (see result section). Following the milling step in IPA, the slurries were left to stabilize for 24 h on a rolling bench before adding the desired amount of acrylate to achieve a solid load between 28 vol% and 36 vol% and evaluate their printability (i.e. rheological properties, cure depth and TG-DSC). Afterwards, the isopropanol was evaporated under constant stirring with a magnetic stirrer and finally the photoinitiator was added. At this stage, the slurries were ready for characterization and additive manufacturing. Three different shapes were printed for the preliminary study: a resolution plate [32], a gyroid and parts with pinholes and knobs with 28 vol% slurry based on HDDA. For the detailed debinding and cracks formation studies, bars were printed (35 mm \times 4.5 mm \times 3.5 mm).

A Lithoz CeraFab 7500 (Lithoz, GmbH, Austria) with a UV ($\lambda = 365 \text{ nm}$) light source was used for DLP-LCM shaping of parts. The vat was filled to have a slurry thickness of about 225 μm . The layer thickness for printing was 25 μm and the X, Y and Z shrinkage compensation was set to 1 (–). The waiting time prior to exposure of subsequent layers was set to 4 s. For cure depth characterization, the irradiance flux density was set to 18.760 mW/cm^2 with exposure times varying from 1 to 7 s. The same irradiance flux density of 18.760 mW/cm^2 was used for the bar printing, adapting only the exposure times depending on the curing characteristics to achieve sufficient cure depth and layer adhesion (for acrylates 0.2 mm and 0.3 mm, for the methacrylate $>0.6 \text{ mm}$). After debinding and sintering, the part dimension shrank to about 28.9 \times 3.8 \times 2.5 mm.

2.3. Characterization methods and procedures

A rheometer (MCR302, Anton Paar, Austria) with a concentric cylinder setup (CC27/T200/SS) was used to characterize the rheological properties of the slurries up to 200 s^{-1} .

Particle size distribution measurements were performed by static light scattering (LS 13320, Beckman Coulter, USA) in isopropanol using Mie scattering for data analysis.

TGA/DTA 851e (Mettler Toledo, USA) was used to determine the thermal decomposition of printed parts up to 800 °C with a heating ramp of 5 °C/min in synthetic air.

Planetary ball milling (Retsch, Germany) with zirconia jars and balls (1 and 3 mm \varnothing) at 300 RPM and different milling times was used for powder milling in IPA and the final slurry homogenization with monomers.

TMA 402 F1/F3 Hyperion (Netzsch, Germany) equipped with a steel furnace, a low-temperature silica measurement setup and a K thermocouple was used to evaluate the shrinkage of printed parts in air.

For debinding and sintering, a PY 12 H 1300 8 (Pyrotec, Germany) and LHT 04/17 with the $T_{\text{max}} = 1750 \text{ °C}$ and 4 L volume (Nabertherm, Germany) furnace were used, respectively. The dwell temperatures for debinding in air were defined based on DSC peak onset temperatures. After debinding, the samples were sintered at 1650 °C for 4 h in air.

The printed parts were observed using optical (Stereo Discovery V20, Zeiss, Germany) and scanning electron (Vega Plus 5136 MM, Tescan, United Kingdom) microscopy.

The density of sintered samples was evaluated following the Archimedes' principle using an A6204 DeltaRange® balance (Mettler Toledo, Switzerland). The mass of the dried sample was recorded (m_1). To fully soak the sample, it was immersed in distilled water and kept under a vacuum until no more bubbling could be observed. After 24 h of soaking, the mass of the sample was measured in water (m_2) and in the air (m_3) after removing excess water from the surface. The apparent density was calculated using the following equation, where $\rho_{\text{H}_2\text{O}}$ is the water density:

$$\rho_{app} = \frac{m_1 \cdot \rho_{H_2O}}{m_3 - m_2} \quad (1)$$

For powder characterization, BET surface area measurement was performed using a SA 3100 (Beckman Coulter, USA) and the crystal structure was evaluated using an X-ray diffractometer (PANalytical X'Pert PRO θ -2 θ , Netherlands) with a Cu $K\alpha_1$ radiation source. The particle size d_{BET} was determined assuming uniform, non-porous and spherical particles:

$$d_{BET} = 6 / (SSA \times \rho) \quad (2)$$

where SSA is the specific surface area and ρ is the density of spinel.

Zeta-potential values as a function of pH were collected with Zeta ProbeTM (Colloidal Dynamics LLC, USA). Titration was carried out using 0.1 M HCl and 0.1 M NaOH in an aqueous suspension with 5 wt% powder content.

3. Results and discussion

3.1. Powder characterization

The measured specific surface area of the powder is 23.1 m²/g, which yields a primary particle size of $d_{BET} = 72.6$ nm, considering spherical particles from SEM imaging (Fig. 1A).

The acid-base properties of the spinel powder were characterized by zeta potential measurements (Fig. 1B), more specifically by determining the isoelectric point (IEP). For spinel powder, the IEP was determined to be at around pH = 10.70, indicating a highly basic character of the powder surface. Considering that organic solvents can either accept or donate a proton and thus act as a base or acid, using the acid/base

dissociation constants (k_A , k_B , $pK = -\log k$), values for acid and based interactions can be calculated (Δ_A , Δ_B) [33], as presented in Fig. 1B.

Measurement of the particle size distribution (Fig. 1C) after 3 min of sonication yielded a $d_{v,50}$ of 2.148 μ m and thus an agglomeration factor of 29 ($F_{ag} = d_{v,50}/d_{BET}$) using 6 as a geometric factor, confirming the strongly agglomerated state of the as-received powder, already observed from the SEM images.

After milling and 24 h of equilibration on the rolling bench, full powder de-agglomeration was achieved, starting from 5 wt% of Sol-spense 41000 (Fig. 1D). To obtain sufficient surface coverage and de-agglomeration (monomodal particle size distribution) while avoiding excessive dispersant amount and possible bridging effects, 5 wt% was chosen as the optimum amount.

3.2. Preliminary AM trials and problem statement

The deagglomeration step allowed achievement of homogeneous microstructures (Fig. 2D) after debinding and sintering of complex-shaped structures (Fig. 2B) from slurries with a solid load of 28 vol% in HDDA. However, dimensional control and resolution were limited to 0.77 mm for pinholes and 0.36 mm for gaps between walls due to extensive light scattering (Fig. 2C). This can be explained by comparing the Mie scattering plots for single particles of 1 μ m and 0.15 μ m of MgAl₂O₄ in HDDA, respectively (Fig. 2F), which reveals that in the current case, a reduction of the particle size leads to an increased lateral scattering intensity, detrimental for the AM process.

SEM analysis of different parts after debinding and sintering (Fig. 3) confirms that the generation of cracks during the debinding process is influenced by the part shape and dimensions. A wall thickness of around 335 μ m in the resolution plate [32] (Fig. 3A and B) does not appear to

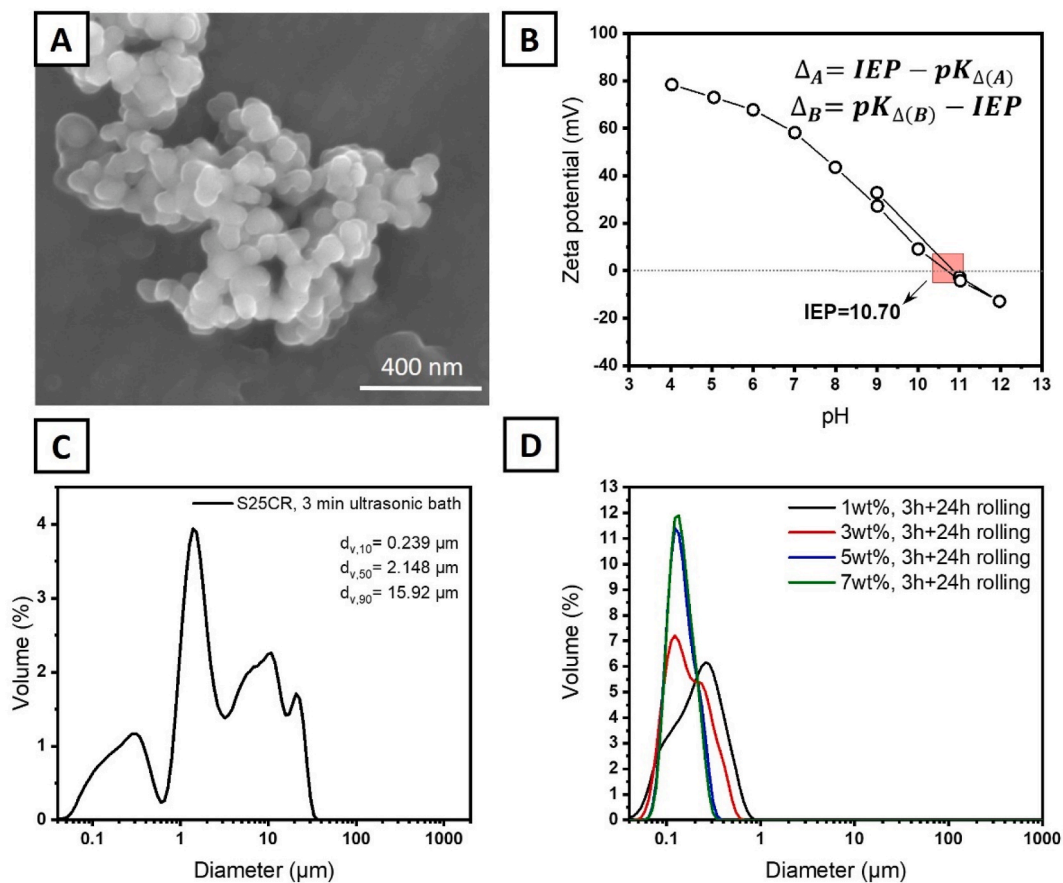


Fig. 1. MgAl₂O₄ powder (A) SEM image, (B) zeta potential in water without the addition of dispersing agent, (C) particle size distribution in water in agglomerated state, (D) particle size distribution in isopropanol after milling 3 h and rolling 24 h for different dispersant amount.

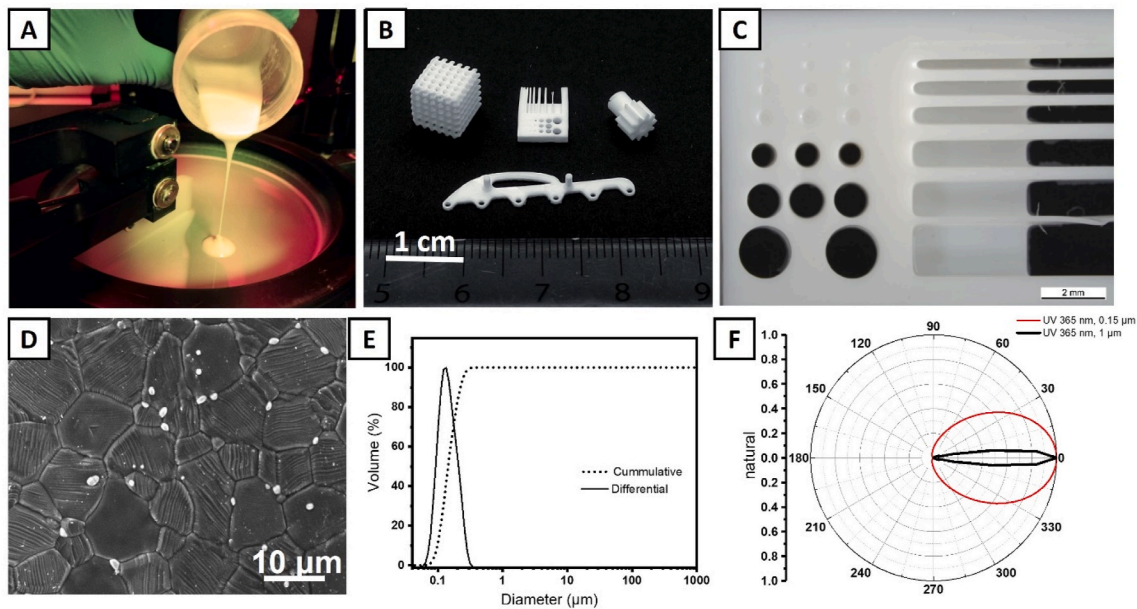


Fig. 2. Powder processing route: (A) slurry with good flow properties and stability, (B) examples of fine complex shape structures, (C) resolution plate after printing, (D) microstructures of printed part as-sintered (E) aggregate-free particle size distribution and, (F) the Mie scattering plots for single particles of 1 μm (black) and 0.15 μm of MgAl_2O_4 (red) in HDDA. (For interpretation of the references to colour in this figure legend, the reader is referred to the Web version of this article.)

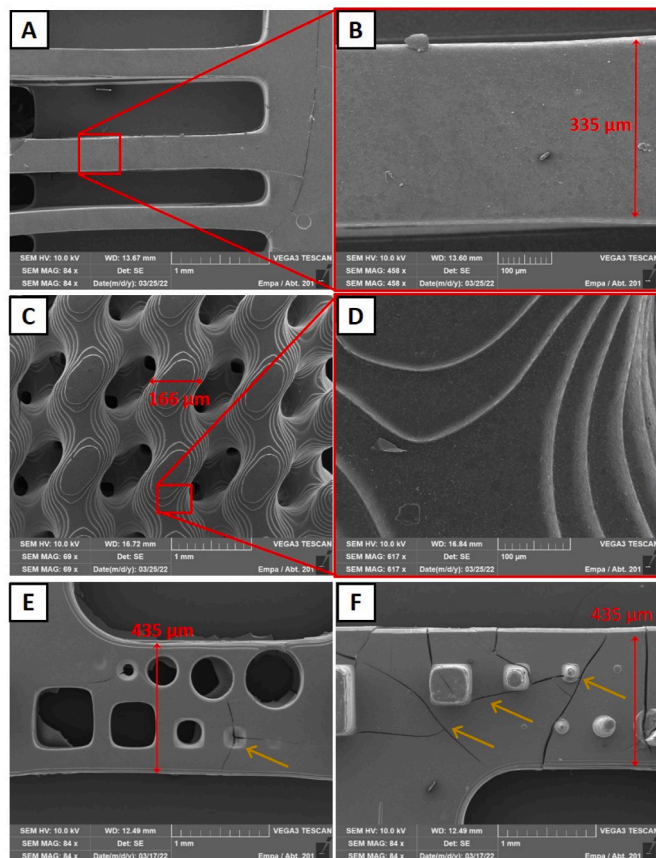


Fig. 3. SEM images of printed parts with the slurry consisting of 28 vol% spinel and HDDA as a monomer (A–B) resolution plate, (C–D) gyroid structure, (E–F) part containing pinholes and knobs.

show a significant density of cracks. Accordingly, also a gyroid structure (Fig. 3C) with a strut thickness of 166 μm usually appears crack-free (Fig. 3D). Further increasing the characteristic part dimensions, a structure (435 μm) with knobs and pinholes starts revealing a moderate number of cracks around the knobs (Fig. 3E) and a very high density of cracks in the solid knob part (Fig. 3F). Thus it can be suggested that in general complex shapes with small bulk volumes, thin walls/struts and the presence of pinholes, tend to inhibit cracking, reducing residual stresses during the AM process (e.g. shrinkage) and facilitating the gas removal during debinding process. True freedom of design in AM hence requires careful management of all process steps to be realized in practice, hence practically limiting the validity of the statement itself.

3.3. Rheology and photocuring behavior of slurries

After slurry formulation from different monomers, their rheological properties, particle size distribution and curing performance were determined and are presented in Table 2. The final viscosity is influenced by the solid loading as well as the viscosity of the pure medium. For example, the high viscosity of TMPTA and DTMPPTA imposes an effective limit of 30 vol% of solid loading for printing. The viscosity for a given solid loading can be estimated based on the Krieger Dougherty relation. Slurries with fine particles, however, tend to have higher viscosity particularly at low shear rates due to significant colloidal interactions. Additionally, none of the slurries presented a yield stress, indicative of the absence of a flocculated state. Based on the power law fitting of shear stress vs shear rate, power law index n indicates $n < 1$ shear thinning for all samples except of DTMPPTA with $n = 1$ indicating Newtonian flow. For methacrylates HDDMA, BDDMA and EGDMA, no curing could be observed within the evaluated energy dose. For the last methacrylate, PEG200DMA, the critical energy dose is high and once exceeded, the cure depth increases rapidly, in agreement with the tendency of methacrylates to form more stable tertiary radicals and thus propagate more slowly (more significant steric hindrance for polymerization) than the secondary radicals formed from acrylates.

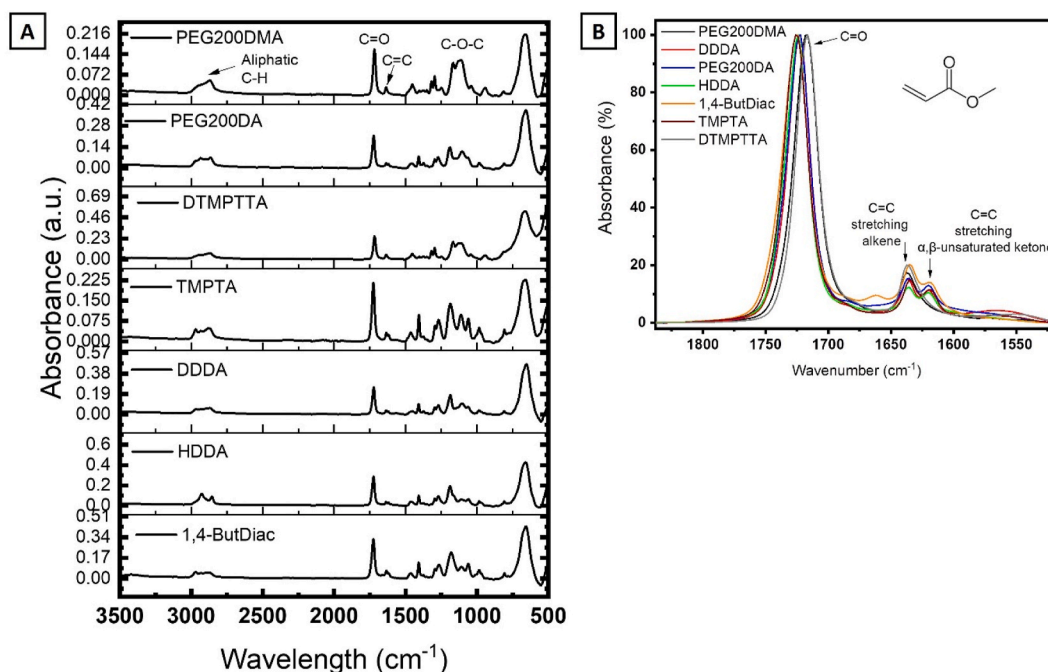
3.4. FTIR analysis after curing

To obtain better insight into the polymerization step, samples were

Table 2

Rheological and curing properties of slurries.

Acrylate	Solid load vol%	Viscosity at 200 s ⁻¹ Pa·s	Energy dose for cure depth 0.2 mm	Energy dose for cure depth 0.3 mm	n value in power law fitting $y = a \cdot x^n$	Flow type based on fitted n value
PEG200DMA	34	1.02	no curing ^a	no curing ^a	0.77	Shear-thinning
PEG200DA	34	1.61	44.086	56.280	0.76	
EGDMA	36	0.39	no curing	no curing	0.72	
BDDMA	35	0.33	no curing	no curing	0.63	
HDDMA	36	0.25	no curing	no curing	0.69	
HDDA	36	2.69	93.800	131.32	0.62	
DDDA	36	2.87	103.180	131.32	0.78	
1,4ButDiac	32	0.28	56.280	69.412	0.76	
TMPTA	30	3.41	50.652	69.412	0.96	
DTMPTTA	29	9.95	44.086	55.800	1	
						Newtonian

^a Curing starts from 140.7 mJ/cm² exceeding cure depth of 0.6 mm.**Fig. 4.** FTIR spectra of cured slurries (A) the whole spectrum in arbitrary units and (B) recalculated to absorbance percentage taken C=O as 100% intensity.

analyzed by FTIR after curing (Fig. 4). All materials show a sharp band around 1720 cm⁻¹ corresponding to C=O bonds present in acrylate and methacrylate functional groups. The band representing C=C double bonds around 1620 cm⁻¹ can be used as a means to evaluate the polymerization degree. Finally, the broad bands around 3000–2800 cm⁻¹ can be attributed to C–H groups and the band around 1100 cm⁻¹ to C–O groups. In order to compare the results more quantitatively, the absorbance spectra were normalized with respect to the C=O band intensity (Fig. 4B). During the polymerization reaction, the amount of C=O bonds in functional groups remained unchanged, while C=C double bonds decreased. Following this approach, low C=C double bond band intensities reflect high polymerization degrees. The observed polymerization degree decreases in the following order: HDDA (12.4%), TMPTA (14.9%), DDDA (15.1%), PEG200DA (15.6%), PEG200DMA (17.5%), DTMPTTA (20.1%) and 1,4-Butanol Diacrylate (20.3%). Note that DTMPTTA and PEG200DMA do not show the second band associated with C=C stretching for unsaturated ketones (alkene double bond conjugated with carbonyl group).

3.5. Debinding analysis by TG-DSC, dilatometry and optical crack analysis

Following the FTIR analysis and determination of double bonds conversion, the thermal decomposition behavior of the presented diacrylates and one dimethacrylate was examined (Fig. 5). For acrylates, the temperature at which thermal decomposition starts is around 300 °C and is accompanied by an exothermal peak between 350 °C and 450 °C. Additionally, a ~9 times smaller exothermal peak can be discerned around 200 °C. Different behavior is observed for PEG200DMA, where mass loss starts already around 250 °C with the accompanying exothermal peak stretching from 250 °C to 450 °C (max. 0.65 mW/mg). It is also preceded by a relatively high exothermal peak around 200 °C (0.35 mW/mg). This suggests that the exothermal process occurring before the main mass loss is much more significant in the case of methacrylate(s) than acrylates. From the total area under the DSC peak at around 200 °C, one obtains 102.1 J/g and 133.7 J/g for PEG200DA and PEG200DMA, respectively. For the second exothermal peak around 400 °C, the values reach 1631 J/g and 845 J/g, respectively. Though this has not been further analyzed, there could be a relation between heat generation and the amount of gaseous product released. The exothermal reaction around 200 °C will be further analyzed in the following

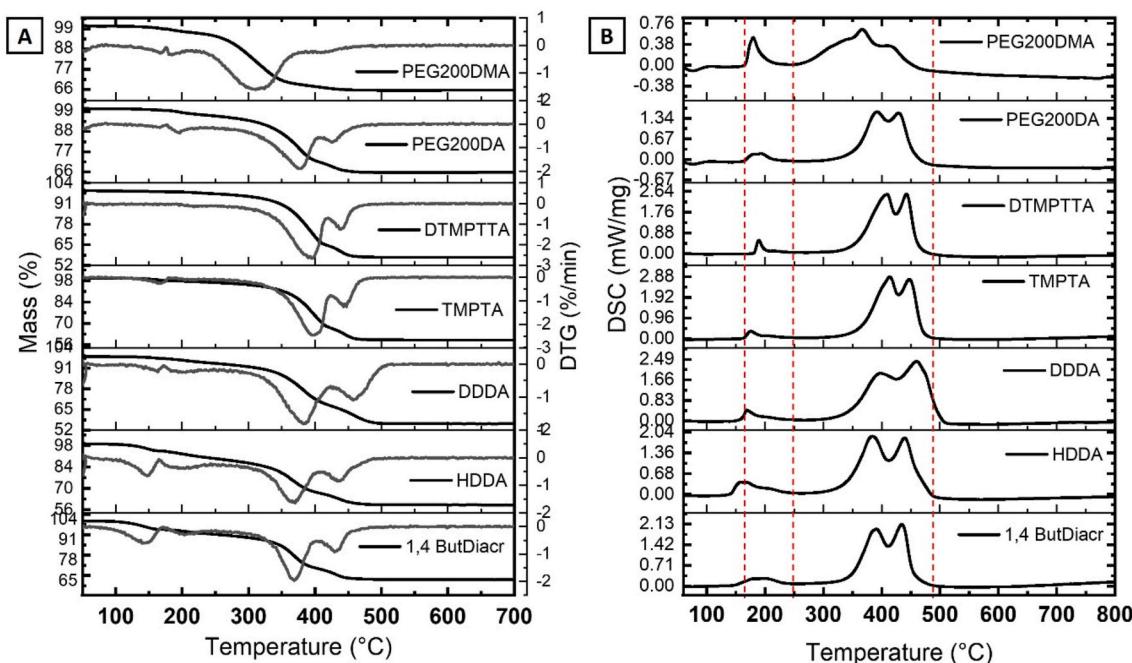


Fig. 5. Thermal decomposition analysis of different acrylates (A) TG, DTG and (B) DSC signals with the red lines to mark slight shifts in the beginning temperature or end temperature of exothermal peaks. (For interpretation of the references to colour in this figure legend, the reader is referred to the Web version of this article.)

sections.

Based on the similarity in curing behavior within the group of acrylates and the group of methacrylates and distinguishably different thermal decomposition behavior for methacrylate only four representative slurries were retained for subsequent debinding analysis, namely PEG200DMA and PEG200DA based on the similarity of chemical structure but different functional group and HDDA and DDDA having different chain length within the group of acrylates to evaluate whether those characteristics impact the debinding behavior. To study the effect of crack formation during the thermal decomposition of HDDA, DDDA, PEG200DA and PEG200DMA, the debinding programs were set according to Table 3 for printed bars and inspected by optical microscope and SEM after sintering. Dwell temperatures were chosen based on the onset of the exothermal peaks (≈ 150 °C, ≈ 300 °C), the temperature of the main mass loss (≈ 400 °C), the end of the main exothermal peak (≈ 500 °C) and finally 800 °C as required for powder calcination as obtained by DSC for each slurry formulation.

Optical microscopy revealed a good surface finish without noticeable presence of delamination for samples made from all four slurries before debinding (Fig. 6). Cracks could be observed for all samples after debinding and sintering. However, the crack network and density differed between samples as it can be observed from the SEM images (right column Fig. 6). For HDDA (Fig. 6A), cracks are mostly formed normal to the layer planes. For DDDA (Fig. 6B), they tend to be long and randomly oriented, while for PEG200DMA (Fig. 6C), a dense crack network is formed with cracks remaining closed (e.g. surfaces in contact). For PEG200DA (Fig. 6D), the situation is completely different with

cracks appearing predominantly in only two directions: parallel and perpendicular to the building direction. It can thus be concluded that the crack formation mechanism in PEG200DMA differs from the crack formation occurring in acrylates, and it may be suggested that this difference is linked to the exothermal processes occurring around 200 °C.

In order to further corroborate the origin of crack formation, the dimension of the bars were measured directly after printing and after debinding + sintering and normalized with the nominal dimension from the CAD file (Fig. 7). Note that accordingly, a negative shrinkage corresponds to blooming (i.e. curing beyond the illuminated area), which scales with the energy dose. The high critical energy dose required for PEG200DMA makes it most susceptible to blooming (Fig. 7C), without a noticeable difference between 140.7 mJ/cm^2 and 159.46 mJ/cm^2 . During the printing step, the shrinkage related to the polymerization reaction mostly is accommodated by height changes, and thus the final shrinkage in the sample heights is significantly higher than in the widths or lengths. It can also be noticed that in all four cases, blooming is more pronounced in width than in length, especially for PEG200DMA. Though this has not been further investigated, it is believed that this is a result of the shear forces applied during the recoating of the vat, which may cause configurational changes (elongation) of long polyethylene glycol chains that may not be fully recovered during the waiting time prior to layer exposure. As consequently curing and relaxation take place simultaneously, blooming may become anisotropic.

3.6. Investigation of the main pyrolysis mechanism

To investigate the contribution of oxidation processes during the decomposition of chosen (meth-)acrylates, TG analysis was carried out in nitrogen and air (Fig. 8). Comparing the results in both atmospheres, differences appear between PEG200DMA and PEG200DA: the mass loss increases for the methacrylate and decreases for the acrylate when moving from air to nitrogen. The higher residual mass in nitrogen is believed to be a consequence of char formation, representative of a higher contribution from the chain scission mechanism rather than depolymerization (e.g. monomer formation). Indeed, acrylic polymers are most likely to undergo chain scission (rather than depolymerization) during pyrolysis, resulting in the production of residual chain fragments,

Table 3
Debinding programs for different slurries.

Heating rate °C/h	Dwell time min	Temp. °C HDDA	Temp. °C DDDA	Temp. °C PEG200DA	Temp. °C PEG200DMA
30	120	140	150	160	160
30	120	300	300	300	250
30	300	400	420	400	400
30	120	490	500	490	490
120	120	800	800	800	800

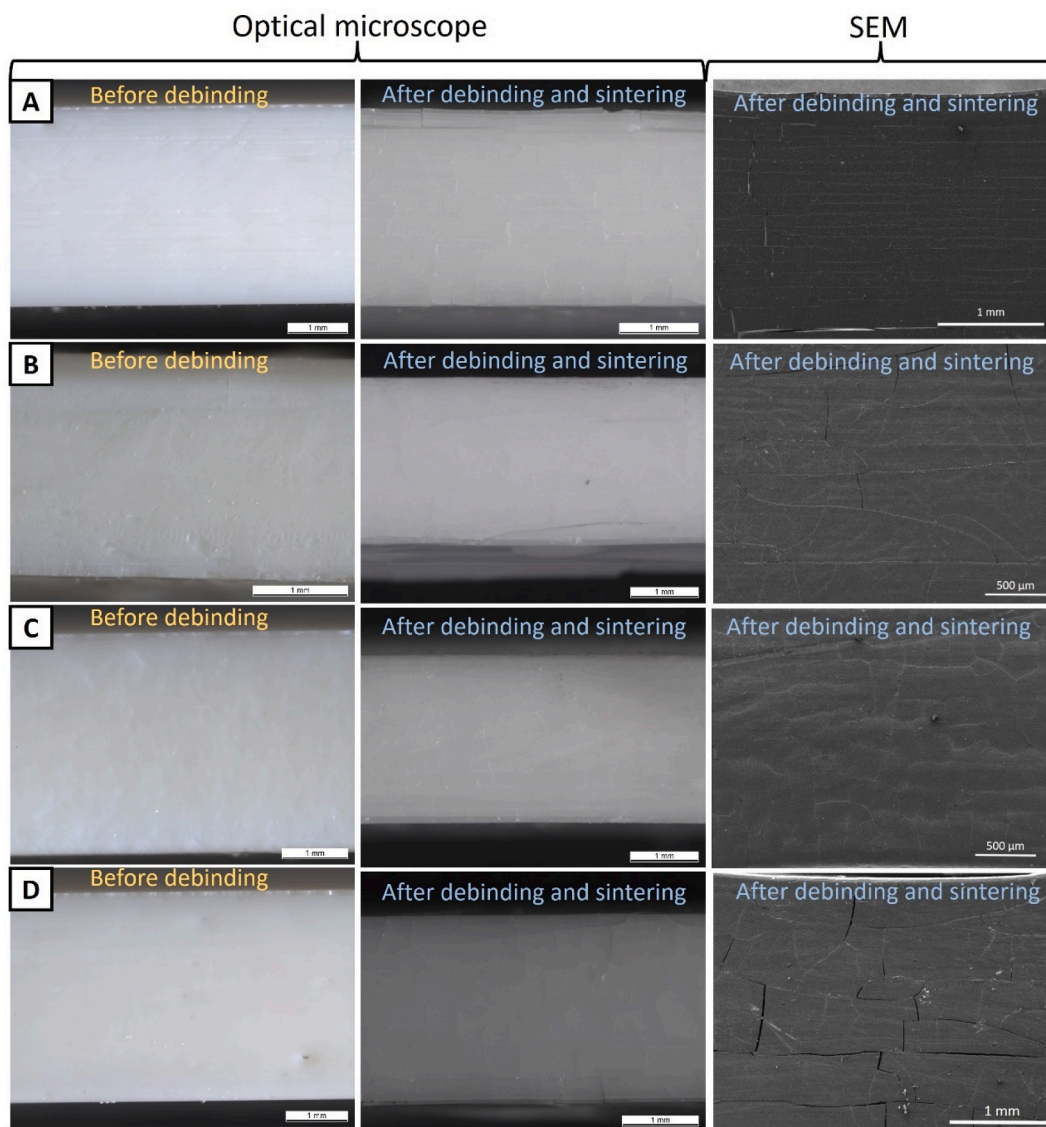


Fig. 6. Optical and SEM images of bars before debinding and after debinding in the sintered state for (A) HDDA 36 vol% 131.32 mJ/cm², (B) DDDA 36 vol% 131.32 mJ/cm², (C) PEG200DMA 34 vol% 159.46 mJ/cm² and (D) PEG200DA 34 vol% 56.28 mJ/cm².

alcohols, olefins and CO₂. Methacrylate polymers, however, most likely undergo depolymerization, resulting in monomer formation (with CO, CO₂, etc.) [34]. In this study, the highest char formation was measured for HDDA, decreasing sequentially for TMPTA, DDDA and PEG200DA. Only PEG200DMA appears to show a lower mass after the pyrolysis in nitrogen compared to air, albeit the profile of the curves remains similar. This is indicative of a reduced contribution from oxidation in the decomposition processes of polymethacrylates. Indeed, this agrees with reports that debinding of poly (methyl methacrylate) in nitrogen results mostly in methyl methacrylate (e.g. monomer) formation, while debinding in air leads to the emission of a significant amount of CO₂ in addition to methyl methacrylate [35]. Finally, it should also be noted that for PEG200DMA, the mass loss curves in air and nitrogen overlap up to 300 °C, a temperature range at which, according to optical images (Fig. 8C and D), the formation of the regular crack network already occurs.

The above can be further corroborated by collating the TG data in nitrogen with the DSC signals in air (Fig. 9A). It appears that the higher residual mass in nitrogen is a consequence of the greater contribution of oxidation during the debinding process (higher DSC in air around 400 °C). Additionally, it may be suggested that the higher the conversion

degree of double bonds in the cured state (Fig. 9B), the higher the residue (e.g., char) formation in nitrogen. The according results are summarized in Table 4.

3.7. Analysis of crack formation

Following the observation of differences in crack formation and TG analysis especially between PEG200DMA and PEG200DA, crack formation was further investigated in the relevant temperature range (up to 200 °C) for acrylates with and without the addition of a non-reactive diluent. Propylene carbonate with a boiling point of 242 °C was used as a non-reactive diluent to evaluate its use as a partial heat sink to mitigate the exothermic reaction within this temperature range and to lower the acrylate content. Although its boiling point is beyond the temperature of interest, propylene carbonate has been selected since its partial pressure and thus evaporation increases with temperature well within the temperature range of interest. Furthermore, exothermic reactions may cause local temperature peaks within the material, well above the set temperature during the TGA analysis.

A combinatorial approach was taken considering both shrinkage (TMA analysis) and heat release (TG-DSC) to investigate the crack

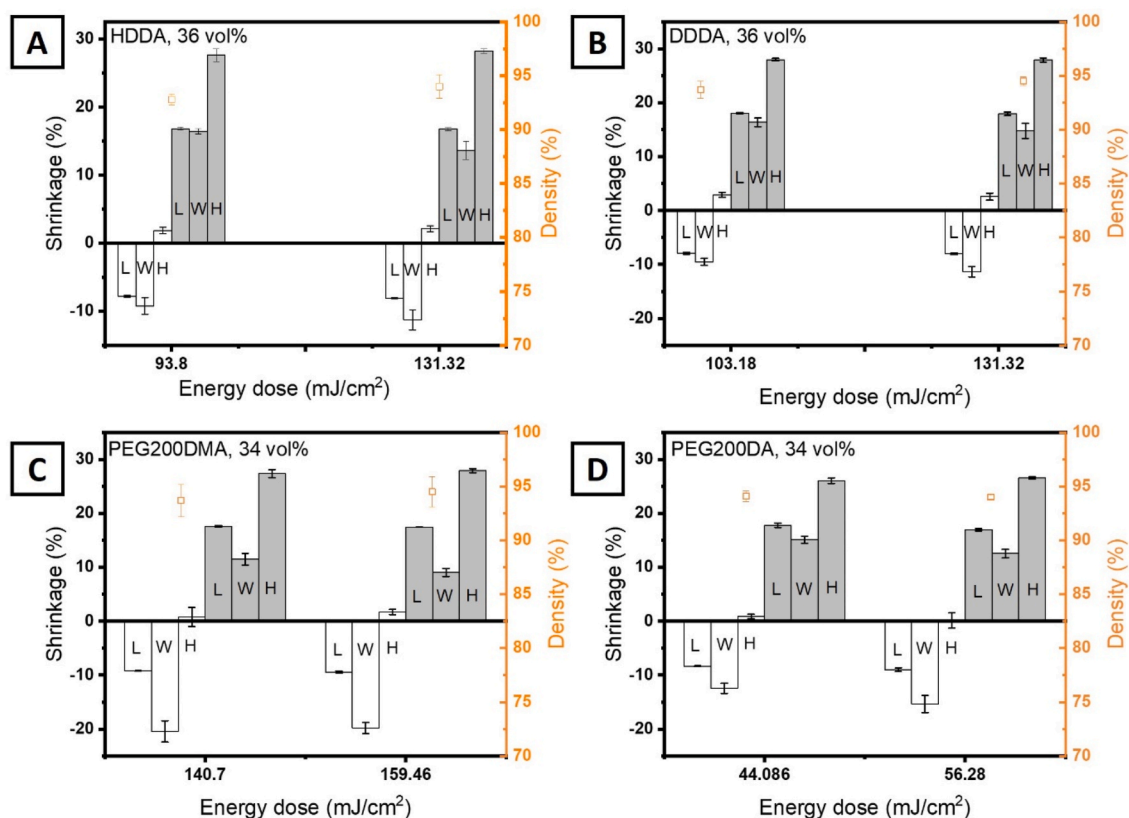


Fig. 7. Shrinkage of bars after printing with maximum solid load before reaching paste properties (white filling) and after debinding and sintering (grey filling) in regards to CAD for (A) HDDA, (B) DDDA, (C) PEG200DMA, (D) PEG200DA, where L – length, W – width, H – height.

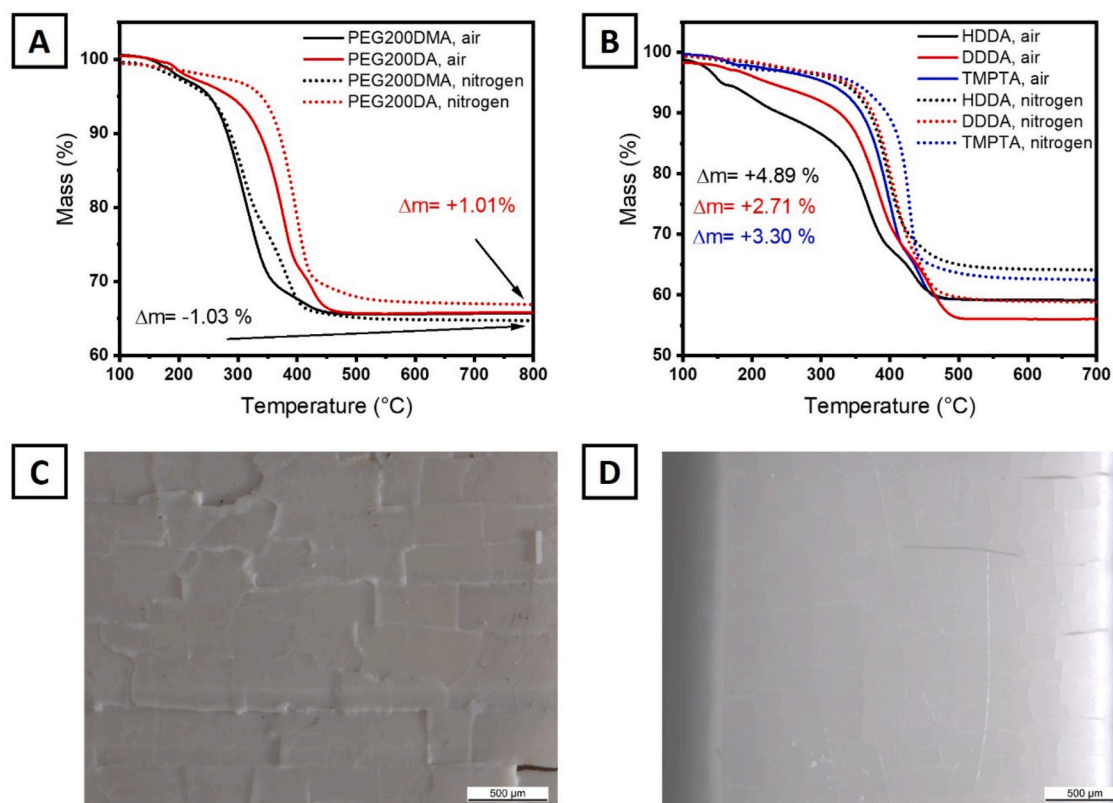


Fig. 8. Mass loss in air and nitrogen for (A) PEG200DMA and PEG200DA, (B) HDDA, DDDA and TMPTA, (C) PEG200DMA after treatment in nitrogen 1 °C/min, 300 °C, dwell time 3 h, (D) PEG200DMA after full debinding in air and sintering.

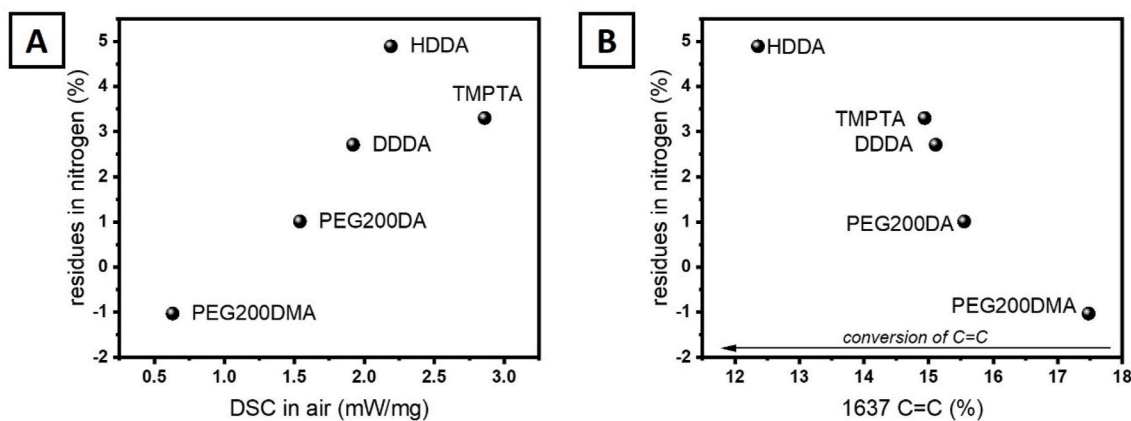


Fig. 9. Comparison of collected data: (A) residues in nitrogen calculated as mass difference between nitrogen and air final mass loss and (B) comparison of $\text{C}=\text{C}$ intensity from FTIR in % with nitrogen residues.

Table 4

Comparison of polymerization degree and the thermal decomposition characteristic features for various acrylates and one methacrylate.

Monomer	1637 cm^{-1} C=C vs 1720 cm^{-1} C=O	Δm nitrogen vs air	DSC $\sim 300^\circ\text{C}$ in air	DSC $\sim 200^\circ\text{C}$ in air	Residue formation in nitrogen	Expected dominating mechanism
	%	%	mW/mg	mW/mg		
PEG200DMA	17.5	-1.03	0.63	0.499	No	Depolymerization
PEG200DA	15.6	1.01	1.54	0.172	Yes	Chain scission
DDDA	15.1	2.71	1.92	0.42	Yes	Chain scission
TMPTA	14.9	3.30	2.86	0.349	Yes	Chain scission
HDDA	12.4	4.89	2.19	0.439	Yes	Chain scission

formation mechanism. To this end, the following sets of samples were evaluated: PEG200DA, PEG200DA+20 vol% propylene carbonate, PEG200DA+15 vol% propylene carbonate, PEG200DMA, PEG200DMA+20 vol% propylene carbonate, and PEG200DMA+15 vol% propylene carbonate. For the manufacturing of the required sample sets, the curing conditions were adjusted for each type to achieve an equivalent cure depth of ~ 0.30 mm.

TMA analysis of PEG200DMA and PEG200DA is presented in Fig. 10. For PEG200DMA, heat treatment up to 200°C results in a small shrinkage after cooling, whereas for PEG200DA, a slight expansion can be observed. After propylene carbonate addition, however, significant shrinkage occurs for all samples, up to 5% in the case of PEG200DMA with 20 vol% propylene carbonate. This suggests that the addition of propylene allows for the parts to deform during thermal treatment, which may be beneficial in avoiding internal stress formation.

FTIR analysis reveals a decrease of $\text{C}=\text{C}$ band intensity around 1620 cm^{-1} after thermal treatment at 200°C (Fig. 11), suggesting that polymerization of residual monomers occurs within the same temperature range.

Optical micrographs of the samples after thermal treatment are presented in Fig. 12. Analysis of the micrographs appears to confirm that the addition of propylene carbonate – and associated plasticity introduction – reveals a shift from a dense crack network formation (Fig. 12D) indicative of large internal stresses towards a coarse crack network formation, as suggested from the dilatometry results.

In order to investigate how the thermo-mechanical property changes relate to calorific changes following the propylene carbonate addition, TG-DSC analysis was also performed, revealing an exothermal peak of around 200°C (Fig. 13) in all cases (pure monomers and monomers with propylene carbonate). For PEG200DMA and PEG200DA, propylene

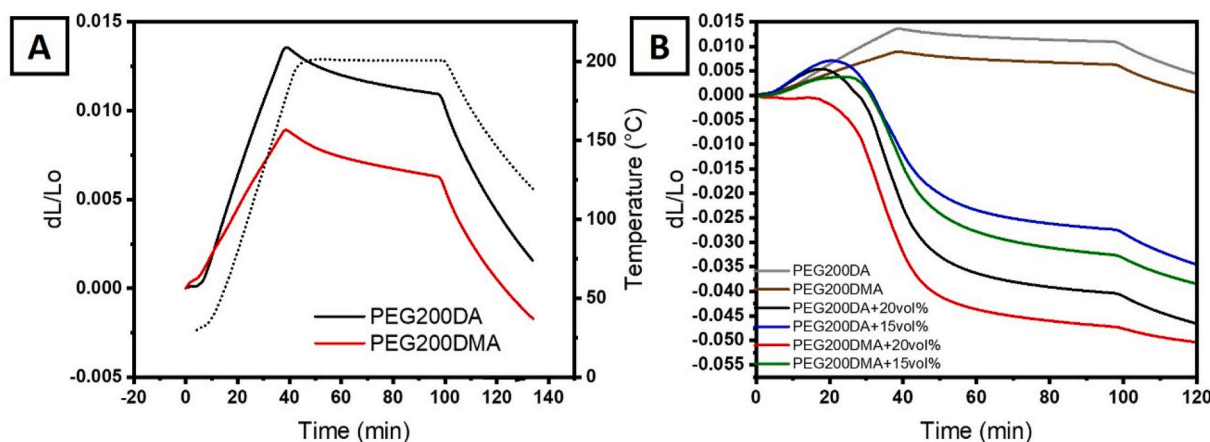


Fig. 10. (A) Thermal shrinkage of bars printed with PEG200DA and PEG200DMA and (B) PEG200DA and PEG200DMA with the addition of Propylene Carbonate 20 vol% and 15 vol%.

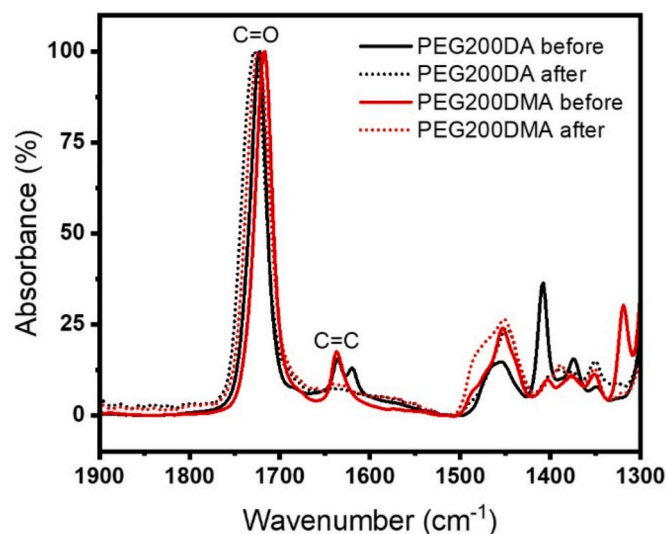


Fig. 11. FTIR before and after thermal treatment for slurries based on PEG200DA and PEG200DMA.

carbonate addition not only leads to a reduction in peak intensities, but also a peak shift towards higher temperatures. Furthermore, it can be observed that the temperature of the DSC peak onset corresponds to the end of the mass loss on the DTG signal. It may thus be suggested that propylene carbonate addition not only reduces heat during evaporation, but also tends to delay the exothermal reaction via local temperature reduction. Interpretation of the results for PEG200DMA are more difficult since polymer decomposition itself occurs at lower temperatures, changing the DSC plot not only quantitatively, but also qualitatively. Indeed, peak overlap analysis reveals the appearance of a new peak, the origin of which is not fully understood. Nonetheless, since the ratio of (meth)acrylate to propylene carbonate is identical and the exothermic peak for PEG200DMA is much more pronounced than for PEG200DA, it may once more be suggested that the reaction has not been fully eliminated and has shifted towards higher temperatures.

To assess the effects of propylene carbonate addition on the exothermal peaks in both cases, a calculation of the reaction enthalpy was performed for the exothermic peaks occurring around 200 °C. The

area under the fitted exothermal peak around 200 °C is represented as a function of the total mass loss in Fig. 14. For both PEG200DA and PEG200DMA, heat release tends to decrease with increasing propylene carbonate addition/evaporation. This suggests that the addition and thus endothermic evaporation of propylene carbonate can at least partially compensate the exothermic heat effect occurring during heat treatment.

3.8. Analysis of photoinitiator concentration impact and post-shaping treatment

Finally, as another means of altering the exothermic peak, the effect of the photoinitiator concentration was investigated. It may influence the polymerization rate and M_w after photocuring and thus shrinkage, double bond conversion and thermal effects during debinding. It should however be noted that a higher concentration of photoinitiator required a reduction of the energy deposition (and thus the cure depth) during curing to avoid excessive blooming/overpolymerization. Dilatometry and FTIR analysis data are presented in Fig. 15. The sample shrinkage (Fig. 15A) tends to increase slightly with the photoinitiator content (PEG200DMA+20 vol% propylene carbonate). C=O peak intensity normalized FTIR spectra (Fig. 15B) reveal that the carboxylic acid group signal around 1800 cm^{-1} is high before and decreases significantly after thermal treatment, without being fully eliminated. In this case, however, the peak around 1640 cm^{-1} (i.e. C=C) does not show significant change for 1, 2 and 3 wt% of the photoinitiator. This suggests that the adjustments required during the curing, especially to avoid blooming, do not significantly alter the shrinkage during the debinding process or conversion degree of C=C bonds. More studies may however be required, especially in combination with the addition of sensitizers and photoinhibitors.

In an attempt to further minimize the effect of residual monomers on debinding, printed samples were pre-treated (before thermal debinding) by post-curing in a UV chamber for 30 min and 2 h for $\lambda = 365$ nm, respectively, or by washing with ethanol in an ultrasonic bath for 2 h (both HDDA and propylene carbonate are soluble in ethanol). As it can be observed from Fig. 17A, all pre-treatment routes led to a reduction of the debinding shrinkage. Ethanol washing in an ultrasonic bath, however, appears to be most efficient in reducing shrinkage. At the energy densities used, no difference could be observed between 0.5 or 2 h of post-curing under UV. FTIR measurements (Fig. 17B) could confirm that

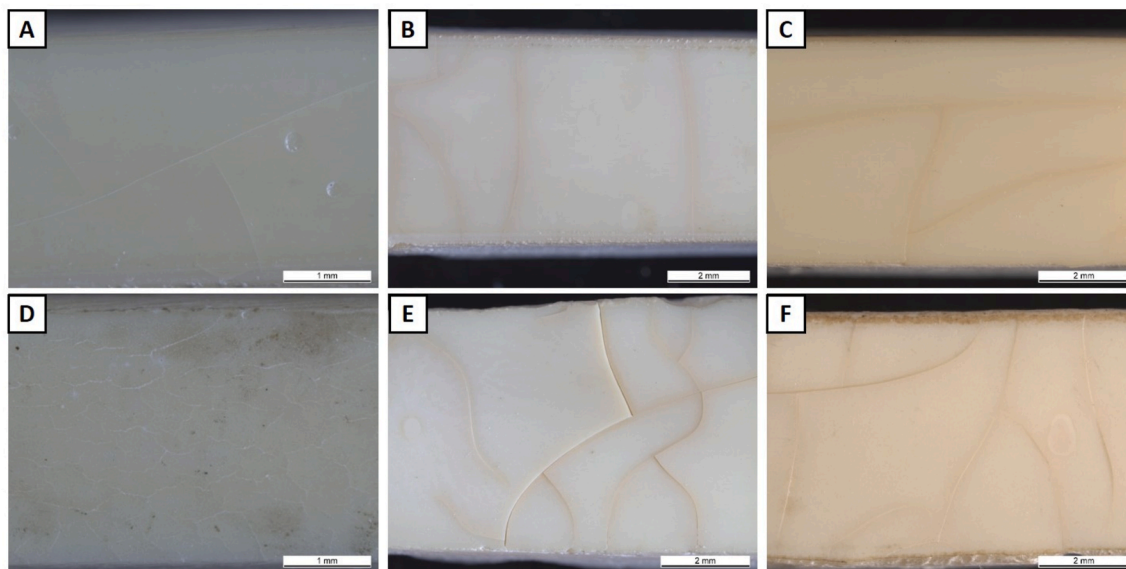


Fig. 12. Optical microscope images after TMA of (A) PEG200DA, (B) PEG200DA+20 vol% propylene carbonate, (C) PEG200DA+15 vol% propylene carbonate, (D) PEG200DMA, (E) PEG200DMA+20 vol% propylene carbonate, (F) PEG200DMA+15 vol% propylene carbonate.

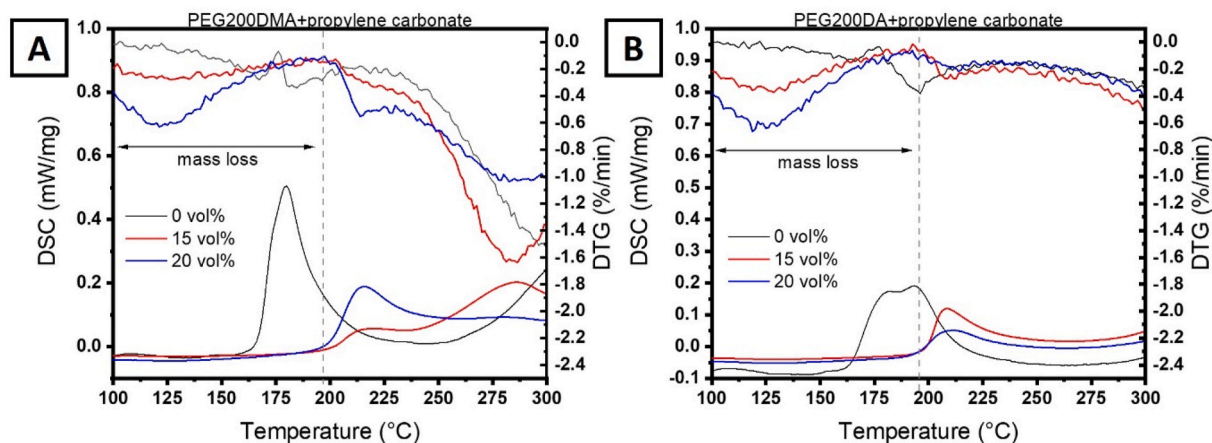


Fig. 13. DSC-DTG graphs for thermal treatment up to 300 °C for (A) PEG200DMA and (B) PEG200DA with propylene carbonate.

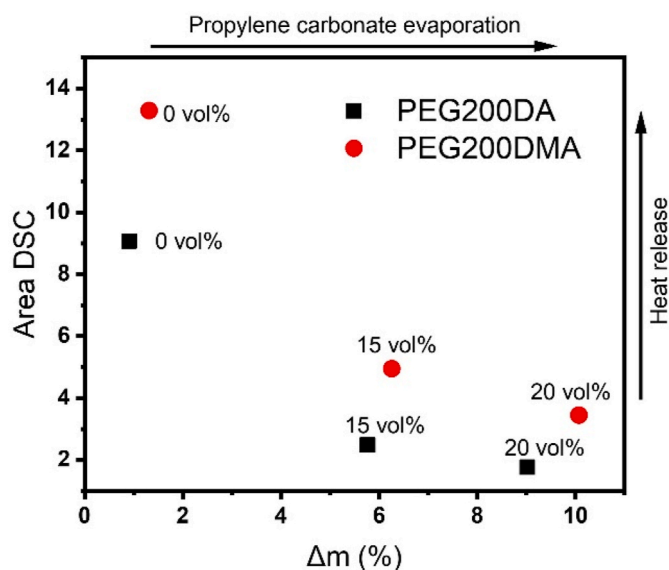


Fig. 14. Correlation between exothermal effect represented as a fitted area under the DSC peak and the mass loss representing evaporation of propylene carbonate.

the band around 1800 cm^{-1} attributed to $\text{C}=\text{O}$ in carboxylic acid decreases for all evaluated pre-treatment methods. The weakest visible band for $\text{C}=\text{O}$ carboxylic groups occurs after US bath treatment, as suggested by the lowest shrinkage observed with this pre-treatment strategy. As the total thermal effect involves different reactions over distinct temperature ranges, the DSC peaks were once more deconvoluted to calculate the area under the peak occurring around 200 °C. The deconvolution results are tabulated with the mass loss in this same temperature range (Fig. 16). Note that TG-DSC analysis was carried out only for UV treatment after 2 h, as there was no measurable difference in shrinkage between treatment for 30 min and 2 h.

Since in this case the strategy directly aims to actually treat/remove non-reacted monomers, the values reveal an opposite trend compared to samples with propylene carbonate with no treatment prior to thermal heating (Fig. 14). For the sample washed in ethanol in a US bath, the exothermal peak was the lowest (5.78), irrespective of the highest removal of propylene carbonate (i.e. only 3.40% mass loss attributable to propylene carbonate evaporation during thermal treatment), which suggests an efficient removal of unreacted monomer during the treatment. This, however, could not be confirmed by FTIR (Fig. 17B), as the ratio between $\text{C}=\text{O}$ and $\text{C}=\text{C}$ bonds remained constant, so the applicability of the suggested normalization method is only valid in case of $\text{C}=\text{C}$ conversion for the constant monomer concentration. UV irradiation, on the other hand, intended to cause a partial $\text{C}=\text{C}$ bond conversion, which could be confirmed by a reduced exothermal effect (8.09) despite post UV-curing being accompanied by partial propylene

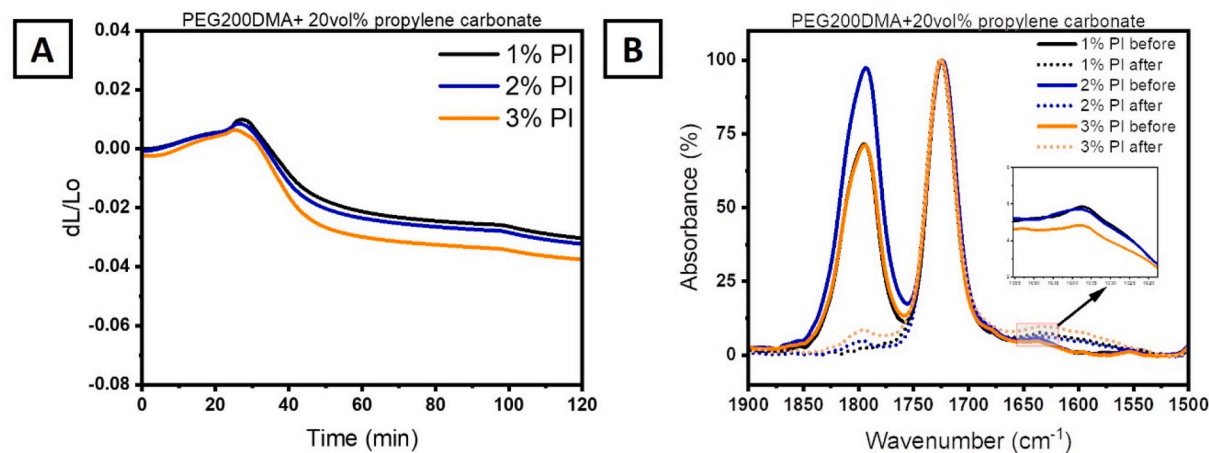


Fig. 15. (A) Shrinkage $\Delta L/L_0$ of the printed bars PEG200DMA+20 vol% propylene carbonate during the thermal treatment in 200 °C with the dwell time 1 h with the heating rate of 5 K/min and (B) FTIR before and after the thermal treatment.

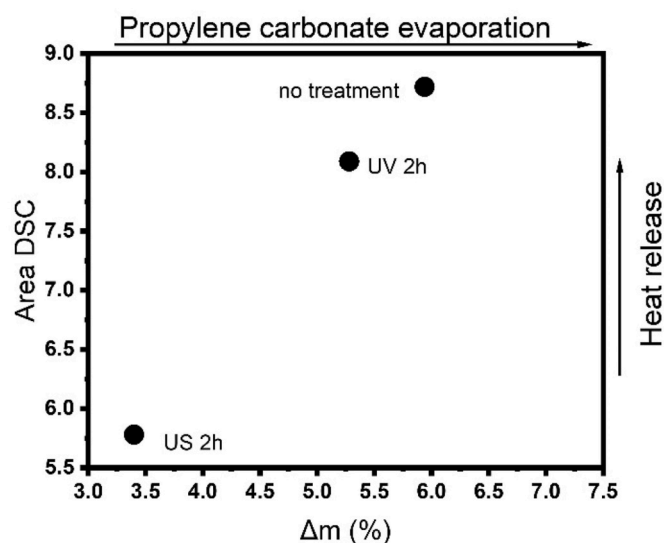


Fig. 16. Comparison of thermal effect and mass loss during heating up to 200 °C for samples without pre-treatment and 2 h of UV irradiation or 2 h of the ultrasonic bath.

carbonate evaporation (i.e. only 5.28% left).

When observing sample cracking (Fig. 17D), further evidence about a positive effect from US bath treatment could be identified. Ethanol washing in a US-bath led to crack alignment perpendicular to the length of the bars (perpendicular to the direction of increased shrinkage as described above) and crack density reduction. Compared to the sample

without the pre-treatment, which exhibits randomly oriented cracks with higher crack density, this suggests that US pre-treatment increases the critical dimension for crack occurrence, which may potentially be further optimized by avoiding shear related configurational inhomogeneities in the slurry prior to photopolymerization. Since US pre-treatment also causes pore generation by propylene carbonate and monomer removal, impregnation with propylene carbonate may be an additional way to further reduce exothermal effects, thereby optimizing the debinding process.

4. Conclusions

This study highlights the challenges remaining in the processing and debinding of AM-shaped parts, especially in combination with sub-micron particle sizes, to satisfy the "free-complexity" promise touted in AM. Indeed, current approaches reveal severe limitations with respect to maximal characteristic sample dimensions (e.g. strut thickness of 166 μm) to prevent crack formation during debinding, especially when dealing with sub-micron particle sizes. Given current trends in the fields towards the use of refined particle sizes, more studies are required to further optimize slurry formulations and debinding processes.

Thermal treatment up to 200 °C of printed parts revealed a decrease of C=C band intensity in FTIR indicative of exothermic residual monomer polymerization. The addition of propylene carbonate as a non-reactive diluent reduces the associated exothermal effect around 200 °C but also retards the reaction up to higher temperatures. Residual monomers cannot be significantly reduced by only varying the amount of photoinitiator (between 1 wt% to 3 wt%). Instead, pre-treatment of PEG200DMA with 20 vol% of propylene carbonate revealed that ethanol washing in an ultrasonic bath allows removal of non-reacted monomers

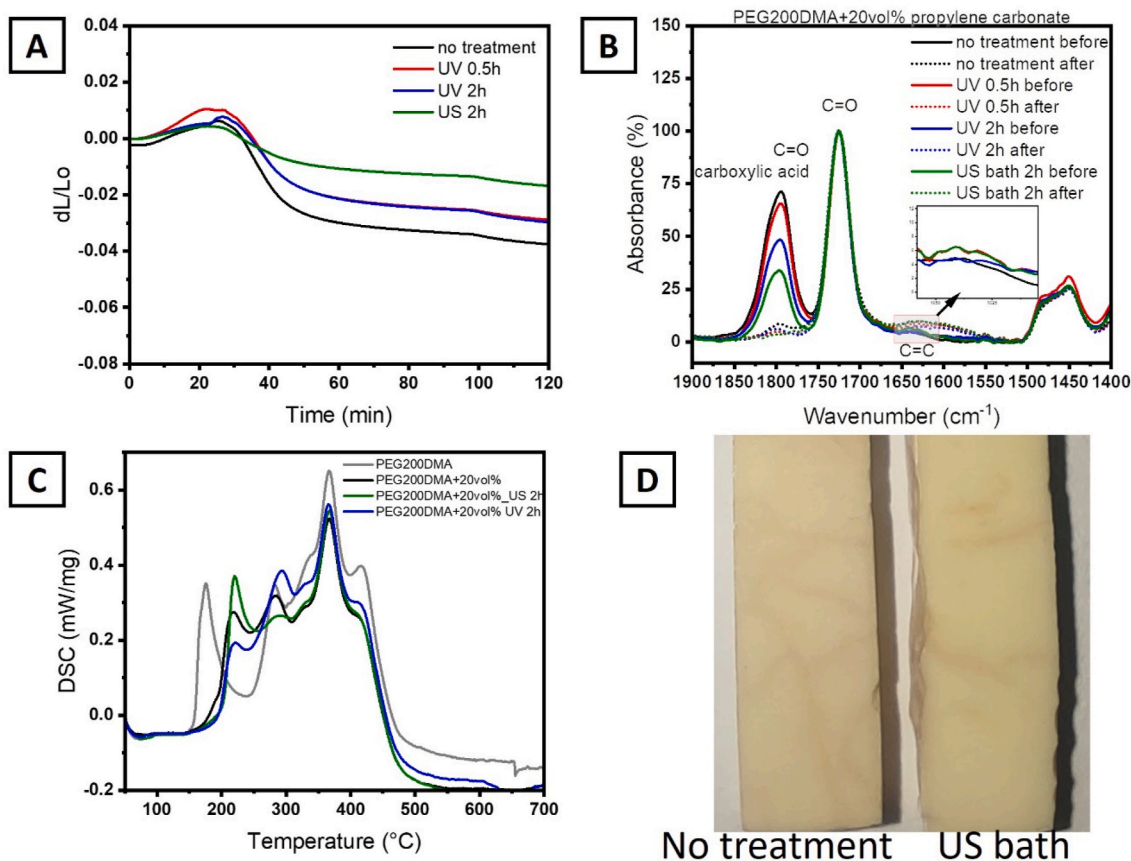


Fig. 17. PEG200DMA+20 vol% propylene carbonate and 3 wt% photoinitiator without pre-treatment and after pre-treatment in an ultrasonic bath in technical ethanol and UV chamber irradiation for 30 min and 2 h (A) shrinkage, (B) FTIR and (C) DSC, (D) samples appearance after TMA shrinkage measurement (top view).

together with propylene carbonate, which is suspected to act as diffusion network generator. By removing both monomers and propylene carbonate jointly, this process allows for reduced exothermal effects during debinding. Refilling of the pore network with propylene carbonate could further improve the crack formation threshold. The alternative approach using UV post-curing was significantly less effective, failing to treat all residual monomer without improving the gas permeability of the green body.

Due to the higher energy dose required for curing and associated reduction in resolution (i.e. overpolymerization/blooming), methacrylates appear to be of limited use in the manufacturing of fine structures. However, due to their reduced heat release during the polymer decomposition (~250–450 °C) and the ability to mitigate their exothermic processes around 200 °C, methacrylates may be more promising for the shaping parts with larger characteristic dimensions.

We propose a combination of two mechanisms that may reduce the formation of cracks during debinding, i.e. the porosity formation and the removal of residual monomer by an ultrasonic bath. The subsequent impregnation with propylene carbonate may further contribute to reducing local overheating and reaction acceleration via exothermic effects with evaporation acting as a heat sink.

Declaration of competing interest

The authors declare that they have no known competing financial interests or personal relationships that could have appeared to influence the work reported in this paper.

Acknowledgements

The authors would like to thank Amir Hadian for providing TG-DSC measurements.

References

- [1] C.-J. Bae, J.W. Halloran, Influence of residual monomer on cracking in ceramics fabricated by stereolithography, *Int. J. Appl. Ceram. Technol.* 8 (6) (2011) 1289–1295.
- [2] O. Santoliquido, F. Camerota, A. Ortona, The influence of topology on DLP 3D printing, debinding and sintering of ceramic periodic architectures designed to replace bulky components, *Open Ceramics* 5 (2021).
- [3] A.K. Hofer, et al., Effect of binder system on the thermophysical properties of 3D-printed zirconia ceramics, *Int. J. Appl. Ceram. Technol.* 19 (1) (2021) 174–180.
- [4] K. Wang, et al., Study on defect-free debinding green body of ceramic formed by DLP technology, *Ceram. Int.* 46 (2) (2020) 2438–2446.
- [5] M. Borlaf, et al., Development of UV-curable ZrO₂ slurries for additive manufacturing (LCM-DLP) technology, *J. Eur. Ceram. Soc.* 39 (13) (2019) 3797–3803.
- [6] A. Goswami, et al., Optimization of rheological properties of photopolymerizable alumina suspensions for ceramic microstereolithography, *Ceram. Int.* 40 (2) (2014) 3655–3665.
- [7] S.Y. Song, et al., Optimization and Characterization of High-Viscosity ZrO₂ Ceramic Nanocomposite Resins for Supportless Stereolithography, *Materials & Design*, 2019, p. 180.
- [8] E. Johansson, et al., Influence of resin composition on the defect formation in alumina manufactured by stereolithography, *Materials* 10 (2) (2017) 1–11.
- [9] Z. Xing, et al., Effect of plasticizer on the fabrication and properties of alumina ceramic by stereolithography-based additive manufacturing, *Ceram. Int.* 44 (16) (2018) 19939–19944.
- [10] H. Li, et al., Effects of solvent debinding on the microstructure and properties of 3D-printed alumina ceramics, *ACS Omega* 5 (42) (2020) 27455–27462.
- [11] J. Kim, et al., Effect of dispersants on structural integrity of 3D printed ceramics, *Int. J. Appl. Ceram. Technol.* 19 (2) (2021) 968–978.
- [12] H. Wu, et al., Effect of the particle size and the debinding process on the density of alumina ceramics fabricated by 3D printing based on stereolithography, *Ceram. Int.* 42 (15) (2016) 17290–17294.
- [13] J. Li, J. Huang, R. Yin, Multistage kinetic analysis of DMAA/MBAM polymer removal from gelcast ceramic parts using a multi-stage parallel reaction model and model-free method, *RSC Adv.* 9 (47) (2019) 27305–27317.
- [14] H. Li, et al., Influence of debinding holding time on mechanical properties of 3D-printed alumina ceramic cores, *Ceram. Int.* 47 (4) (2021) 4884–4894.
- [15] M. Zhou, et al., Preparation of a defect-free alumina cutting tool via additive manufacturing based on stereolithography – optimization of the drying and debinding processes, *Ceram. Int.* 42 (10) (2016) 11598–11602.
- [16] H. Wang, et al., 3D printing of transparent spinel ceramics with transmittance approaching the theoretical limit, *Adv. Mater.* (2021), e2007072.
- [17] H. Li, et al., Effect of debinding temperature under an argon atmosphere on the microstructure and properties of 3D-printed alumina ceramics, *Mater. Char.* (2020) 168.
- [18] J. Zhang, et al., Digital light processing-stereolithography three-dimensional printing of yttria-stabilized zirconia, *Ceram. Int.* 46 (7) (2020) 8745–8753.
- [19] L. Zhang, et al., Effects of debinding condition on microstructure and densification of alumina ceramics shaped with photopolymerization-based additive manufacturing technology, *Ceram. Int.* 48 (10) (2022) 14026–14038, <https://doi.org/10.1016/j.ceramint.2022.01.288>. In press.
- [20] Z. Chen, et al., 3D printing of ceramics: a review, *J. Eur. Ceram. Soc.* 39 (4) (2019) 661–687.
- [21] Y. Lakhdar, et al., Additive manufacturing of advanced ceramic materials, *Prog. Mater. Sci.* 116 (2021).
- [22] S. Zakeri, M. Vippola, E. Levänen, A comprehensive review of the photopolymerization of ceramic resins used in stereolithography, *Addit. Manuf.* 35 (2020).
- [23] Y. De Hazan, et al., High solids loading ceramic colloidal dispersions in UV curable media via comb-polyelectrolyte surfactants, *J. Colloid Interface Sci.* 337 (1) (2009) 66–74.
- [24] X. Wu, et al., Influence of boundary masks on dimensions and surface roughness using segmented exposure in ceramic 3D printing, *Ceram. Int.* 45 (3) (2019) 3687–3697.
- [25] J. Sun, J. Binner, J. Bai, Effect of surface treatment on the dispersion of nano zirconia particles in non-aqueous suspensions for stereolithography, *J. Eur. Ceram. Soc.* 39 (4) (2019) 1660–1667.
- [26] R.-J. Huang, et al., Fabrication of complex shaped ceramic parts with surface-oxidized Si₃N₄ powder via digital light processing based stereolithography method, *Ceram. Int.* 45 (4) (2019) 5158–5162.
- [27] K. Zhang, et al., Digital light processing of 3Y-TZP strengthened ZrO₂ ceramics, *Mater. Sci. Eng., A* (2020) 774.
- [28] P. Zubrzycka, et al., Metal cation complexes as dispersing agents for non-aqueous powder suspensions, *Ceram. Int.* 47 (13) (2021) 18443–18454.
- [29] S.P. Gentry, J.W. Halloran, Depth and width of cured lines in photopolymerizable ceramic suspensions, *J. Eur. Ceram. Soc.* 33 (10) (2013) 1981–1988.
- [30] Y. Li, et al., Critical thickness in binder removal process for injection molded compacts, *Mater. Sci. Eng., A* 362 (1–2) (2003) 292–299.
- [31] A. Eibel, E. D. Fast, and G. Gescheidt, Choosing the ideal photoinitiator for free radical photopolymerizations: predictions based on simulations using established data, *Polym. Chem.* 9 (41) (2018) 5107–5115.
- [32] L. Conti, et al., Effects of the layer height and exposure energy on the lateral resolution of zirconia parts printed by lithography-based additive manufacturing, *Materials* 13 (6) (2020).
- [33] J.C. Bolger, Acid base interactions between oxide surfaces and polar organic compounds, in: K.L. Mittal (Ed.), *Adhesion Aspects of Polymeric Coatings*, Springer US, Boston, MA, 1983, pp. 3–18.
- [34] P.K. Johnston, E. Doyle, R.A. Orzel, Acrylics: a literature review of thermal decomposition products and toxicity, *J. Am. Coll. Toxicol.* 7 (2) (1988) 139–200.
- [35] K.L. Erickson, Thermal Decomposition of Polymers in Nitrogen and in Air, *International SAMPE Technical Conference*, 2007.